Explicit Thermochemical Nonequilibrium Algorithm Applied to Compute Three-Dimensional Aeroassist Flight Experiment Flowfields

Grant Palmer*

NASA Ames Research Center, Moffett Field, California 94035

This study presents a three-dimensional explicit, finite-difference, shock-capturing numerical algorithm applied to viscous hypersonic flows in thermochemical nonequilibrium. The algorithm employs a two-temperature physical model. Equations governing the finite-rate chemical reactions are fully coupled to the gas dynamic equations using a novel coupling technique. The new coupling method maintains stability in the explicit, finite-rate formulation while allowing relatively large global time steps. The code uses flux-vector splitting to difference the inviscid fluxes to second-order accuracy. Comparisons with experimental data and other numerical computations verify the accuracy of the present method. The code is used to compute the three-dimensional flowfield over the Aeroassist Flight Experiment vehicle at one of its trajectory points.

Nomenclature

c_s	= mass fraction of species s
D_{sj}	= binary diffusion coefficient
e	= total energy per unit volume
e_v	= vibrational energy per unit volume
$\hat{e}_v$	= vibrational energy per unit mass
$\hat{F},\hat{G},\hat{H}$	= inviscid flux vectors
g_0, g_1	= degeneracy factors
h_s^0	= heat of formation of species s
h_s	= static enthalpy of species s
k_f, k_b	= forward and backward rate constants
K_{eq}	= equilibrium constant
M	= molar mass
p	= pressure
$\hat{Q}$	= vector of conservative variables
q_v	= vibrational heat conduction
R	= universal gas constant
Re	= Reynolds number, $\rho_\infty c_\infty l / \mu_\infty$
$\hat{S}$	= viscous flux vector
T	= translational temperature
T_v	= vibrational temperature
t	= time
U,V,W	= flow velocities in ξ,η,ζ directions
U_s,V_s,W_s	= diffusion velocities in ξ,η,ζ directions
u,v,w	= flow velocities in x,y,z directions
u_s,v_s,w_s	= diffusion velocities in x,y,z directions
$\hat{W}$	= source term vector
$\bar{w}$	= chemical source term
X_s	= mole fraction
x,y,z	= Cartesian coordinate directions
β	= real-gas equation of state parameter
κ	= thermal conductivity
μ	= viscosity
Ω	= collision integral
ρ	= density
σ	= collision diameter
θ_1, θ_2	= characteristic temperature of electronic excitation
θ_d	= characteristic temperature of dissociation
θ_{vs}	= characteristic temperature of vibration
ξ,η,ζ	= generalized coordinate directions

Introduction

THE Aeroassist Flight Experiment (AFE) vehicle, a major element of NASA's Civilian Space Technology Initiative, is scheduled for launch in 1994. Released from the Space Shuttle, the AFE will pass through the Earth's atmosphere and be recovered by the Shuttle. The primary purposes of AFE are to demonstrate the viability of aerobraking as a means of planetary entry and to gather experimental data that will be used to validate real-gas computational fluid dynamic (CFD) codes.

The AFE will travel in the Earth's upper atmosphere at velocities ranging from 7–10 km/s. At these conditions both chemical and thermal nonequilibrium effects will be significant. It is impossible to duplicate this flow regime in ground-based test facilities. Design of the AFE will depend on numerical techniques to approximate the aerodynamic and thermal loads it will experience. Newly developed real-gas Navier Stokes codes will be used along with older boundary-layer and viscous shock-layer techniques to design the AFE heat shield as well as the experiments that will be carried aboard the spacecraft.

This study outlines the development of a three-dimensional, shock-capturing, fully coupled, finite-rate thermochemical nonequilibrium algorithm. The code uses a two-temperature physical model to compute the dissociation, ionization, and the thermochemical nonequilibrium effects in the high temperature region behind the bow shock. Numerical solutions generated with the code are compared against experimental and computational data. A three-dimensional flowfield about the AFE at one of its flight trajectory points is then calculated.

Governing Equations

The three-dimensional Navier-Stokes equations, including species continuity equations, represent the conservation of mass, momentum, and energy. The equations are usually transformed into a generalized, body-oriented (ξ,η,ζ) coordinate system. In the thin-layer simplification, only the ζ-derivative viscous terms are considered, where ζ is the direction perpendicular to the body surface. Particularly for the three-dimensional flow, the thin-layer assumption greatly simplifies the formulation of the conservation equations in generalized coordinates. The three-dimensional, thin-layer Navier-Stokes

equations in generalized coordinates in vector form are

$$\frac{\partial \hat{Q}}{\partial t} + \frac{\partial \hat{F}}{\partial \xi} + \frac{\partial \hat{G}}{\partial \eta} + \frac{\partial \hat{H}}{\partial \zeta} = \frac{1}{Re}\frac{\partial \hat{S}}{\partial \zeta} + \hat{W} \tag{1}$$

where

$$\hat{Q} = J^{-1}\begin{bmatrix} \rho_1 \\ \cdot \\ \cdot \\ \rho_s \\ \rho \\ \rho u \\ \rho v \\ \rho w \\ e \\ e_v \end{bmatrix} \qquad \hat{F} = J^{-1}\begin{bmatrix} \rho_1[U+U_1] \\ \cdot \\ \cdot \\ \rho_s[U+U_s] \\ \rho U \\ \rho uU + \xi_x p \\ \rho vU + \xi_y p \\ \rho wU + \xi_z p \\ (e+p)U \\ e_v U \end{bmatrix}$$

$$\hat{G} = J^{-1}\begin{bmatrix} \rho_1[V+V_1] \\ \cdot \\ \cdot \\ \rho_s[V+V_s] \\ \rho V \\ \rho uV + \eta_x p \\ \rho vV + \eta_y p \\ \rho wV + \eta_z p \\ (e+p)V \\ e_v V \end{bmatrix} \qquad \hat{H} = J^{-1}\begin{bmatrix} \rho_1[W+W_1] \\ \cdot \\ \cdot \\ \rho_s[W+W_s] \\ \rho W \\ \rho uW + \zeta_x p \\ \rho vW + \zeta_y p \\ \rho wW + \zeta_z p \\ (e+p)W \\ e_v W + \Sigma e_{vs} W_s \end{bmatrix}$$

$$\hat{S} = J^{-1}\begin{bmatrix} 0 \\ \cdot \\ \cdot \\ \cdot \\ 0 \\ 0 \\ K_1 u_\zeta + \zeta_x K_2 \\ K_1 v_\zeta + \zeta_y K_2 \\ K_1 w_\zeta + \zeta_z K_2 \\ K_1(\kappa T_\zeta + K_3) + K_2 W - \Sigma_s \rho_s W_s h_s \\ -q_v \end{bmatrix}$$

$$\hat{W} = J^{-1}\begin{bmatrix} \bar{w}_1 \\ \cdot \\ \cdot \\ \bar{w}_s \\ 0 \\ 0 \\ 0 \\ 0 \\ 0 \\ \Sigma \bar{w}_s \hat{e}_{vs} + \Sigma Q_{T-V_s} \end{bmatrix}$$

with

$$U = \xi_x u + \xi_y v + \xi_z w \qquad U_s = \xi_x u_s + \xi_y v_s + \xi_z w_s$$

$$V = \eta_x u + \eta_y v + \eta_z w \qquad V_s = \eta_x u_s + \eta_y v_s + \eta_z w_s$$

$$W = \zeta_x u + \zeta_y v + \zeta_z w \qquad W_s = \zeta_x u_s + \zeta_y v_s + \zeta_z w_s$$

$$K_1 = \mu(\zeta_x^2 + \zeta_y^2 + \zeta_z^2) \qquad K_2 = \tfrac{1}{3}\mu(\zeta_x u_\zeta + \zeta_y v_\zeta + \zeta_z w_\zeta)$$

$$K_3 = u_\zeta u + v_\zeta v + w_\zeta w$$

The Jacobian is given by

$$J = \left[x_\xi(y_\eta z_\zeta - y_\zeta z_\eta) - x_\eta(y_\xi z_\zeta - y_\zeta z_\xi) + x_\zeta(y_\xi z_\eta - y_\eta z_\xi) \right]^{-1}$$

The equation set consists of s species mass equations, a total mass equation, three momentum equations, a total energy equation, and a vibrational energy equation. By definition, the sum of the species densities is equal to the total density. Some methods leave one species density out of the equation set and solve for it by subtracting the remaining species densities from the total density. This concentrates any numerical errors in the species that is omitted. In this study, all the species densities are solved. The resulting mass fractions are scaled so as to equal one insuring that the sum of the species densities equals the total density. This process spreads any numerical error among all the species.

A general gas in thermal nonequilibrium would be characterized by a translational, rotational, and electron temperature as well as a vibrational temperature for each diatomic and polyatomic species present. To simplify this model, the translational and rotational temperatures are assumed to equilibrate quickly. Further, one vibrational temperature characterizes the vibrational state of all diatomic and polyatomic species, and the electron temperature is equal to this vibrational temperature. Therefore, this two-temperature model[1] consists of one translational and one vibrational temperature. Two energy equations, total and vibrational, must be solved.

An equation relating the total energy and translational temperature is

$$e = 1.5RT\sum_s \frac{\rho_s}{M_s} + RT\sum_m \frac{\rho_s}{M_s} + e_v + e_{el}$$
$$+ \tfrac{1}{2}\rho(u^2 + v^2 + w^2) + \sum_s \rho_s h_s^0 \tag{2}$$

The first two terms are the energy of translation and rotation. The vibrational energy is related to the vibrational temperature by the equation for a harmonic oscillator

$$e_v = \sum_m \frac{\rho_s R}{M_s} \frac{\theta_{vs}}{e^{\theta_{vs}/T_v} - 1} \tag{3}$$

The summation Σ_m in Eqs. (2) and (3) signifies that only molecules are considered in evaluating rotational and vibrational energy. A Boltzmann distribution is assumed of electronic states characterized by the vibrational temperature T_v. Of the seven species considered, the energy of electronic excitation is significant only for atomic nitrogen, atomic oxygen, and diatomic oxygen. It is given by the expression

$$e_{el} = \sum_{n,0,0_2} \frac{\rho_s R}{M_s} \left[\frac{\theta_1 g_1 e^{-\theta_1/T_v} + \theta_2 g_2 e^{-\theta_2/T_v}}{g_0 + g_1 e^{-\theta_1/T_v} + g_2 e^{-\theta_2/T_v}} \right] \tag{4}$$

The pressure can be related to the other global conservation quantities by the relation

$$p = (\beta - 1)\left[e - \tfrac{1}{2}\rho(u^2 + v^2 + w^2) \right] \tag{5}$$

The quantity β is used in the flux splitting. Its determination will be discussed in a subsequent section.

Energy Exchange Mechanism and Heat Conduction

The rate of energy exchange between the vibrational and translational modes is taken from Park[1]

$$Q_{T-V_s} = \frac{e_{vs}^*(T)-e_{vs}}{\tau_{vs}} \left| \frac{T_{shk}-T_v}{T_{shk}-T_{vshk}} \right|^{S_s-1} \quad (6)$$

This is a modified form of the Landau-Teller formulation. The quantity $e_{vs}^*(T)$ is the vibrational energy evaluated using the translational temperature. The postshock translational and vibrational temperatures are T_{shk} and T_{vshk}. The postshock vibrational temperature is taken to be the freestream temperature.[2] The relaxation time τ_{vs} is the sum of the Landau-Teller relaxation time and a collision limited relaxation time that corrects for the fact that the Landau-Teller relaxation rate is unrealistically high at high temperatures.[1] The quantity within the brackets in Eq. (6) is an empirical bridging function that accounts for the diffusive nature of the energy exchange that occurs at high vibrational temperatures.

An expression for the vibrational heat conduction in the x direction is

$$q_{vx} = -\mu \frac{\partial \hat{e}_v}{\partial x} \quad (7)$$

with similar expressions for q_{vy} and q_{vz}. This is similar to the expression of energy transport from Vincenti and Kruger.[3]

Transport Properties

Calculating multicomponent diffusion is a complicated and computationally intensive process. As a simplification, the binary diffusion model was used in this study. The diffusion mass flux of species s can be expressed by[4]

$$\rho_s u_s = \frac{-\rho(1-c_s)}{\sum_{j \neq s} \frac{X_j}{D_{sj}}} \frac{\partial c_s}{\partial x} \quad (8)$$

with similar expressions for $\rho_s v_s$ and $\rho_s w_s$. The velocity in Eq. (8) is in units of cm/s. The binary diffusion coefficient for each species pair can be calculated from[4]

$$D_{sj} = 0.0026280 \frac{T^{1.5}}{p\sigma_{sj}^2 \Omega_{sj}^{(1,1)*}} \sqrt{\frac{M_s+M_j}{2M_sM_j}} \quad (9)$$

A close approximation to the values obtained from Eq. (9) can be obtained from a curve fit using the expression

$$D_{sj} = \frac{AT^B}{p} \quad (10)$$

where p in Eqs. (9) and (10) is the pressure in atmospheres. The parameters A and B were chosen to match the diffusion coefficient from Eq. (9) at temperatures of 200 and 10,000 K and showed close agreement over the entire temperature range. Values of A and B for the seven species are listed in Table 1.

Table 1　Diffusion coefficients

Species pair	A	B
N_2—O_2	1.338e-05	1.682
N—O	2.480e-05	1.682
N—NO	1.874e-05	1.684
N—N_2	1.979e-05	1.673
N—O_2	1.914e-05	1.682
O—NO	1.655e-05	1.696
O—N_2	1.866e-05	1.678
O—O_2	1.705e-05	1.695
NO—NO^+	1.129e-05	1.705
NO—N_2	1.321e-05	1.684
NO—O_2	1.176e-05	1.70

A considerable simplification to Eq. (8) can be achieved if the diffusion coefficient is assumed constant. This is acceptable if the constituents of the gas are of similar molecular weight and have similar values of σ and $\Omega^{(1,1)*}$. Electrons have a much lower molecular mass than any of the other constituents, but the mole fractions of electrons are considered low enough in the flows considered in this work to be neglected. Equation (8) becomes[5]

$$\rho_s u_s = -\rho \frac{1-c_s}{1+X_s} D \frac{\partial c_s}{\partial x} \quad (11)$$

where D is some average value of the diffusion coefficients.

The viscosity of a gas mixture can be calculated using Wilke's mixing rule[6]

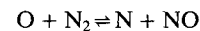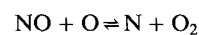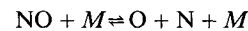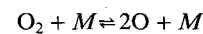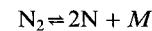$$\mu = \sum_s \frac{\mu_s}{1 + \frac{1}{X_s} \sum_{j \neq s} X_j \phi_{sj}} \quad (12)$$

with

$$\phi_{sj} = \frac{\left[1 + \left(\frac{\mu_s}{\mu_j}\right)^{0.5} \left(\frac{M_j}{M_s}\right)^{0.25}\right]^2}{\sqrt{8}\left[1 + \frac{M_s}{M_j}\right]^{0.5}} \quad (13)$$

where μ_s is the viscosity of a pure gas. The mixture thermal conductivity can be expressed in a similar fashion[7]
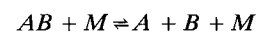
$$\kappa = \sum_s \frac{\kappa_s}{1 + \frac{1.065}{X_s} \sum_{j \neq s} x_j \phi_{sj}} \quad (14)$$

Chemical Model

The chemical reactions considered in this study were

$$N_2 \rightleftharpoons 2N + M$$

$$O_2 + M \rightleftharpoons 2O + M$$

$$NO + M \rightleftharpoons O + N + M$$

$$NO + O \rightleftharpoons N + O_2$$

$$O + N_2 \rightleftharpoons N + NO$$

$$N + O \rightleftharpoons NO^+ + e^- \quad (15)$$

The impacting body M in the first three reactions can be any one of the species. The chemical model therefore consists of seven species and 24 reactions. For a sample reaction[3]

$$AB + M \rightleftharpoons A + B + M$$

the rate of change of the molar density of AB is

$$\frac{d[AB]}{dt} = -k_f[AB][M] + k_b[A][B][M] \quad (16)$$

The forward and backward reaction rates are of the form

$$k_f(T) = C_f T^{\eta_f} e^{-\theta_d/T} \qquad k_b(T) = \frac{k_f(T)}{K_{eq}(T)} \quad (17)$$

The first three reactions in Eq. (15) are heavy-particle impact dissociation reactions. The forward rate is dependent on the vibrational excitation of the diatomic molecule and the kinetic energy of the impacting particle. The temperature that governs the forward reaction rate is taken to be the geometric average of the translational and vibrational temperatures[1]

$\sqrt{TT_v}$. The reverse reaction is dependent on the relative velocities of the impacting particles and is governed only by the translational temperature.

Reactions four and five are exchange reactions among neutral species. The forward and backward rates are assumed to be governed only by the relative velocities of the impacting particles and hence only on the translational temperature. The forward rate of reaction six will also only depend on the translational temperature, but the reverse rate will depend on the vibrational temperature of NO^+ and the translational temperature of the electron both of which in the two-temperature model are equal to the vibrational temperature T_v.

The equilibrium constants were found using the equation[8]

$$K_{eq}(T) = \exp(A_1 + A_2 z + A_3 z^2 + A_4 z^3 + A_5 z^4) \qquad (18)$$

where

$$z = 10,000/T$$

Spatial Differencing

The differencing used in the present algorithm is attributed to Van Leer.[9] The technique splits and differences the inviscid fluxes according to the direction of signal propagation. The mass fluxes are continuously differentiable through a sonic point. For supersonic regions, there is no splitting. The entire flux is either forward or backward differenced according to the flow direction. For subsonic flow, the fluxes are split into forward and backward components. A generalized three-dimensional Van Leer split flux vector is given by

$$\hat{F}^\pm, G^\pm, H^\pm = Ke_1^\pm \begin{bmatrix} 1 \\ \dfrac{k_1}{K\beta}(\pm 2c - \bar{u}) + u \\ \dfrac{k_2}{K\beta}(\pm 2c - \bar{u}) + v \\ \dfrac{k_3}{K\beta}(\pm 2c - \bar{u}) + w \\ \dfrac{2c^2 \pm 2(\beta-1)\bar{u}c - (\beta-1)\bar{u}^2}{\beta^2 - 1} + \dfrac{u^2 + v^2 + w^2}{2} \end{bmatrix} \qquad (19)$$

where

$$K = \sqrt{k_1^2 + k_2^2 + k_3^2}$$

for $F^\pm$:

$$k_1 = \xi_x, k_2 = \xi_y, k_3 = \xi_z \qquad e_1^\pm = \pm\frac{\rho}{4c}\mu(\bar{u} \pm c)^2 \qquad \bar{u} = U/K$$

for $G^\pm$:

$$k_1 = \eta_x, k_2 = \eta_y, k_3 = \eta_z \qquad e_1^\pm = \pm\frac{\rho}{4c}(\bar{u} \pm c)^2 \qquad \bar{u} = V/K$$

for $H^\pm$:

$$k_1 = \zeta_x, k_2 = \zeta_y, k_3 = \zeta_z \qquad e_1^\pm = \pm\frac{\rho}{4c}(\bar{u} \pm c)^2 \qquad \bar{u} = W/K$$

The density in the flux vectors is scaled by the Jacobian, and c is defined by

$$c = \sqrt{(\beta p/\rho)} \qquad (20)$$

This form is similar to the ideal gas equation for sound speed with β replacing the ratio of specific heats γ. The velocity c given in Eq. (20) is not in general the nonequilibrium sound speed but yields consistent split flux vectors. Second-order accurate spatial differencing is desirable for proper resolution of the boundary layer. First-order differencing is necessary in regions of strong gradients, such as a shock, to eliminate oscillations that could cause the solution to go unstable. A transition operator that smoothly switches from second- to first-order accuracy or vice versa was developed in a previous study.[10]

Initial and Boundary Conditions

The numerical solutions were all impulsively started, i.e., initially the flow was freestream everywhere. Freestream values were maintained along the supersonic inflow boundary. The outflow boundary was also assumed to be supersonic, and zeroth-order extrapolation from the interior was used. The no-slip condition and zero normal pressure gradient were imposed on the wall. However, the solution progressed more rapidly if a normal momentum wall boundary condition was employed during the first several hundred steps. The wall was assumed to be noncatalytic.

Along the singular line extending from the nose outward, a simple extrapolation/averaging boundary condition was used. This is not a numerically rigorous boundary condition and caused some problems in the stagnation region of the three-dimensional flowfield. This boundary condition worked best if there was no cross flow through the singular line.

Chemistry Coupling

The algorithm described in this study is fully coupled, meaning the species and global conservation equations are solved simultaneously. The inclusion of species conservation equations with chemical source terms has two effects; it greatly increases the size and complexity of the matrices to be filled and inverted if an implicit method is used and it makes the equation set "stiff" if an explicit method is employed.

The order of the implicit matrices increases as the square of the number of equations solved. For fully coupled, three-dimensional, implicit algorithms, this can mean memory requirements larger than possible for all but the largest supercomputers to provide. This has forced many using implicit techniques[5,11,12] to use Gauss-Seidel, point-implicit, or semi-implicit techniques. Even with these methods, three-dimensional, fully coupled, implicit codes tend to be large and complex, and developing or modifying them can be an arduous task.

Stiffness in explicit fully coupled codes arises from the fact that the source terms in the species continuity equations can sometimes be large relative to the other flux terms. Small time steps are required to keep the solution stable and to prevent nonphysical species densities from occurring. The advantage of the explicit formulation lies in its simplicity. The code is significantly easier to develop and modify. Explicit codes are

ideally suited for patched grid systems over complex shapes such as the AFE. Explicit codes also require substantially less memory.

In a previous study,[10] a technique was developed that overcame the stiffness problem with the explicit finite-rate formulation. Relating change in mass fraction to change in species density

$$\delta(\rho_s) = \delta(c_s\rho) = c_s\delta\rho + \rho\delta c_s \tag{21}$$

or

$$\delta c_s = \frac{\delta\rho_s - c_s\delta\rho}{\rho} \tag{22}$$

the procedure is as follows.

1) Obtain the changes in species density $\delta\rho_s$ by solving the species conservation equations. The species mass fluxes are split exactly as the global mass flux except ρ_s is used instead of ρ.

2) Calculate the changes in species mass fraction δc_s using Eq. (22). The changes in mass fraction are used instead of $\delta\rho_s$ because by definition mass fraction is always between zero and one. Note that for consistency in Eq. (22), the ρ in the denominator is the updated value $\rho^{n+1} = \rho^n + \delta\rho$ obtained from solving the conservation of global density equation, and the c_s in the numerator is c_s^n.

3) Find the maximum δc_s, and if its magnitude is greater than a prescribed tolerance, scale the changes in mass fractions.

$$\delta c_s = \frac{\delta c_s}{|\delta c_{\max}|} * tol \tag{23}$$

The value tol is the maximum amount any species mass fraction is permitted to change per time step. A typical value of tol is 0.01. This scaling also preserves the relative magnitudes of the changes in mass fractions δc_s.

4) Update the mass fractions.

$$c_s^{n+1} = c_s^n + \delta c_s \tag{24}$$

5) Update the species densities.

$$\rho_s^{n+1} = c_s^{n+1}\rho^{n+1} \tag{25}$$

This under-relaxation process limits the rate at which the gas can dissociate and ionize and prevents wild swings in mass fractions and temperature. The gas gradually and stably relaxes to its steady-state composition and temperature. The effect of the scaling can also be thought of as reducing the chemistry time step while maintaining a high global time step. The explicit code can be run at global time steps corresponding to Courant numbers of 0.5 to 0.9, comparable to those possible with a perfect gas code.

The value of the under-relaxation parameter tol is somewhat arbitrary, but there is an upper limit. If tol is set too high in the initial stages of a flow solution, the chemical state of the gas oscillates, and the solution never converges. If tol is set too low, the dissociation of the gas is excessively restricted, and more steps are required to reach steady state.

The updated species densities are used in an iterative process to compute the translational and vibrational temperatures of the gas. The vibrational temperature is obtained from Eq. (3) using the vibrational energy obtained from solving the vibrational energy conservation equation, and the translational temperature is calculated using Eq. (2). Once the temperatures are determined, pressure is calculated using the equation $p = \rho RT$. Finally, the quantity β can be found by

$$\beta = 1 + \frac{p}{e - \frac{1}{2}\rho(u^2 + v^2 + w^2)} \tag{26}$$

Code Validation

A series of test cases were identified to compare results generated by the present code against experimental and numerical data. The experimental results include ballistic range and flight data. In the first test case, the numerical comparisons are made with results produced by Candler.[2,13] Candler used a two-dimensional, fully coupled, implicit code with a more sophisticated multitemperature chemical model. It included the seven species used in this study but considered a translational and electron temperature and a separate vibrational temperature for each of the four diatomic species. Candler's multitemperature code takes significantly more CPU time to produce a solution than the explicit code presented in this work and has not been extended to three dimensions but has compared well against a variety of experimental data. Comparisons against Candler's results around axisymmetric bodies should provide a good test of the accuracy of the present work.

Case A: RAMC II Flight Experiment

The first case duplicated the RAMC II flight experiment. The RAMC II vehicle was a 15-cm, nose radius, 9 deg, half-angle cone with an overall length of 130 cm. Peak electron density along the body was inferred from measurements taken at several altitudes along its trajectory.[14] For both Candler's calculations and the present work, the wall temperature was held fixed at 1500 K.

Figure 1 shows results for the RAMC II vehicle at 61 km traveling at Mach 23.9. Figure 1a compares stagnation line values of temperature computed by Candler and those by the present work. The values of translational temperature and shock standoff distance are very similar between the two methods. The four vibrational temperatures computed by Candler were close to one another. The T_v for molecular nitrogen is shown in Fig. 1a. The vibrational temperature computed using the two-temperature model lies between the vibrational and electron temperatures computed by the multitemperature model as would be expected.

Figure 1b shows values of density normalized by the freestream density along the stagnation line. The densities predicted by the two codes are coincident. Figure 1c shows species distributions along the stagnation line. Freestream mass fractions for N_2 and O_2 used in the present work were 0.7656 and 0.2344, respectively, corresponding to freestream mole fractions of 0.7885 and 0.2115. Candler used slightly different freestream mass fractions.

The calculated species distributions are similar. There are some differences at the wall, which may be attributed to different grid spacing near the wall or to different levels of boundary layer dissipation inherent in the two schemes. The amount of dissociation of N_2 and O_2 is dictated by the geometric mean temperature $\sqrt{TT_v}$. A two-temperature model will in general predict a lower vibrational temperature than the case where the vibrational and electron temperatures are considered separately. Because of this one would expect a greater amount of nitrogen dissociation to be predicted by Candler. This effect is seen in Fig. 1c.

The peak electron number density along the body is plotted in Fig. 1d. There is enough uncertainty in the experimental data to say that both codes do a reasonable job predicting the peak electron density. One difference between the computed and experimental results is that the noncatalytic boundary condition causes the computed peak electron number density to occur at the wall while the experimental profiles show the peak near the shock. The computed electron number densities near shock were 30 to 40% lower than the experimental values. However, the fact that the two different computational methods can produce similar results over different grids is encouraging.

Case B: Shock Detachment on Spheres

The next case involved comparison against measured shock detachment distances on spheres performed at the U.S. Naval
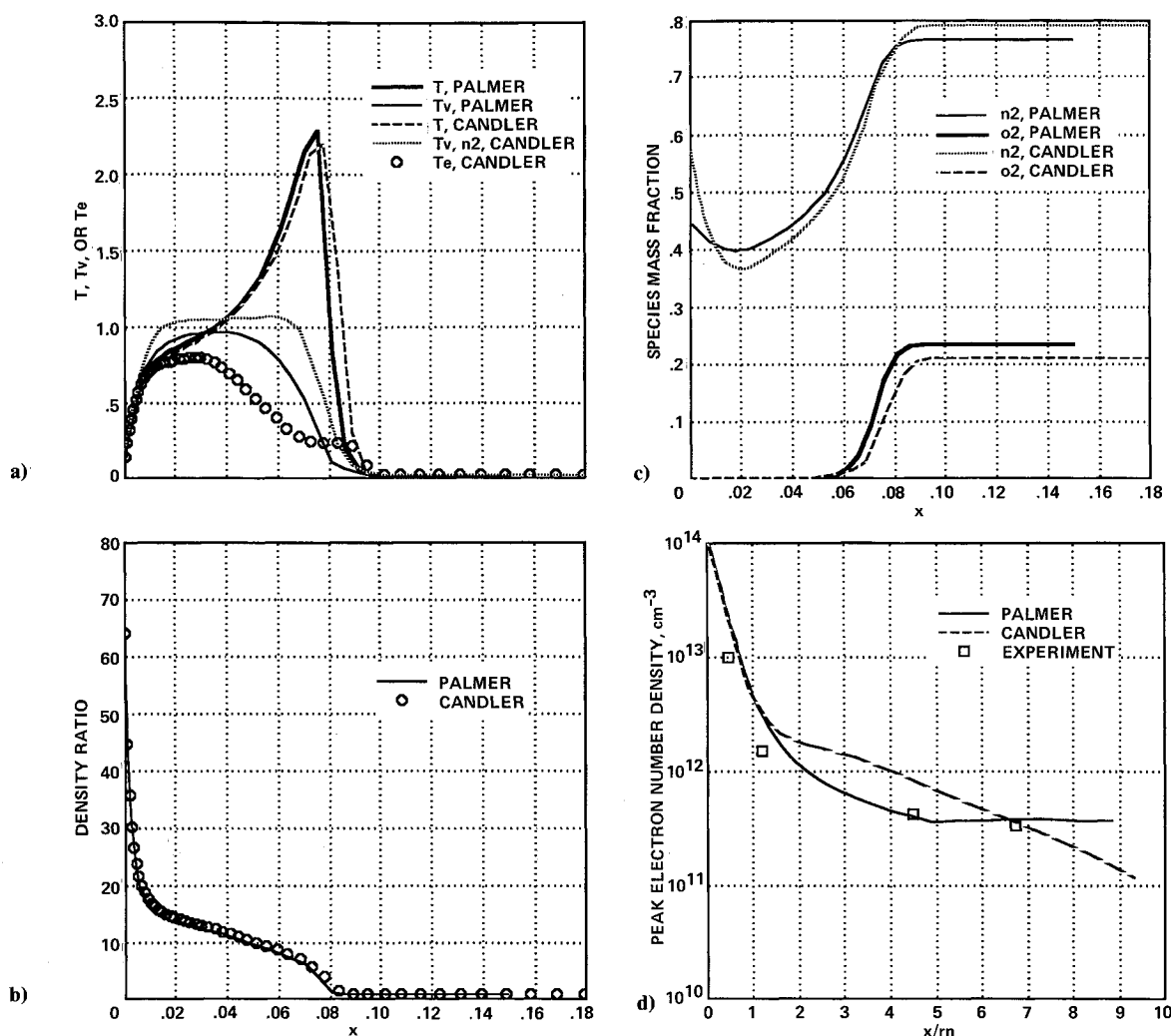
Fig. 1 RAMC II vehicle at 61 km, stagnation line values: a) temperatures; b) normalized density; c) species mass fractions, N_2 and O_2; and d) peak electron number density.

Ordnance Laboratory.[15] The sphere diameter was 0.5 in., the ambient air pressure was 10-mm Hg, and the freestream temperature was 293 K. Computations were done at two velocities, 14,000 and 18,000 fps using the two-temperature code and a one-temperature chemical nonequilibrium code presented previously.[16] Figure 2 shows normalized density plots produced by the two codes for the 18,000 fps case that indicate the computed shock standoff. Included on the plot is the experimentally determined standoff distance with the range of error estimated by Lobb.[15] The numerical results indicate the one- and two-temperature codes predicted very similar shock standoffs slightly higher than the experimental values. That the codes predicted similar standoffs is reasonable because at these flight conditions thermal nonequilibrium effects would be expected to be small.

A sensitivity study was undertaken to determine whether the value of the parameter *tol* influences the final solution or the convergence rate. Flow was computed over the RAMC II vehicle at Mach 23.9 and 61-km altitude. Three values of *tol* were used ranging from 0.01–0.0001. The same time step was used for each calculation. Virtually no differences in the final solution were apparent when different values of *tol* are used indicating that the value of the parameter *tol* does not influence the final solution.

There was a difference in the rate of convergence between the *tol* = 0.0001 case and the other two. A smaller value of *tol* means the species mass fractions can change less per time step, and the gas dissociates more slowly. When the value of *tol* is too small, the shock overexpands off the body and must con-
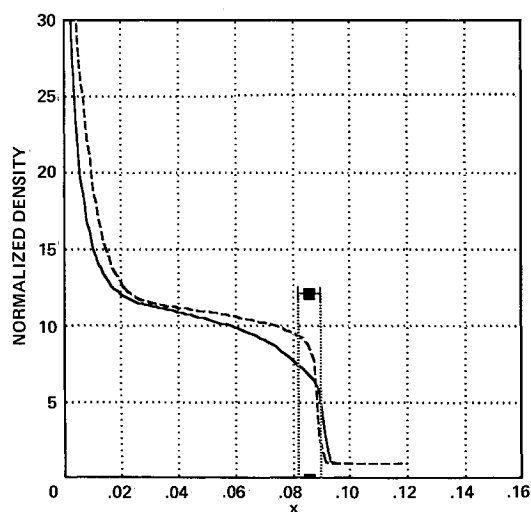

Fig. 2 Shock standoff distance comparison, Mach 15.96, $v = 18,000$ fps.

tract in before a steady state can be reached. In effect, the chemistry lags the fluid dynamics at the beginning of a flow solution. If *tol* is too small, more time steps are required to complete a solution which is wasteful of CPU time. For the RAMC II 61-km case with *tol* = 0.0001, the shock actually hit the outer edge of the grid after 1600 steps and then later moved

back in to its proper steady-state location. An additional 600 time steps were required before the solution coincided with the other two cases. In general, it is recommended that *tol* be set as high as possible. A suggested value is 0.01.

The residuals normally drop about three orders of magnitude and then approach an asymptotic limit. The chemistry coupling appears to introduce a low-level oscillation in the

flow solution, which prevents convergence to machine zero. An examination of the solutions when this point is reached reveals that the shock location is fixed, and thermodynamic quantities examined at various grid points change by only small amounts. The solutions are converged in the sense that

O EXPERIMENT, KRUSE

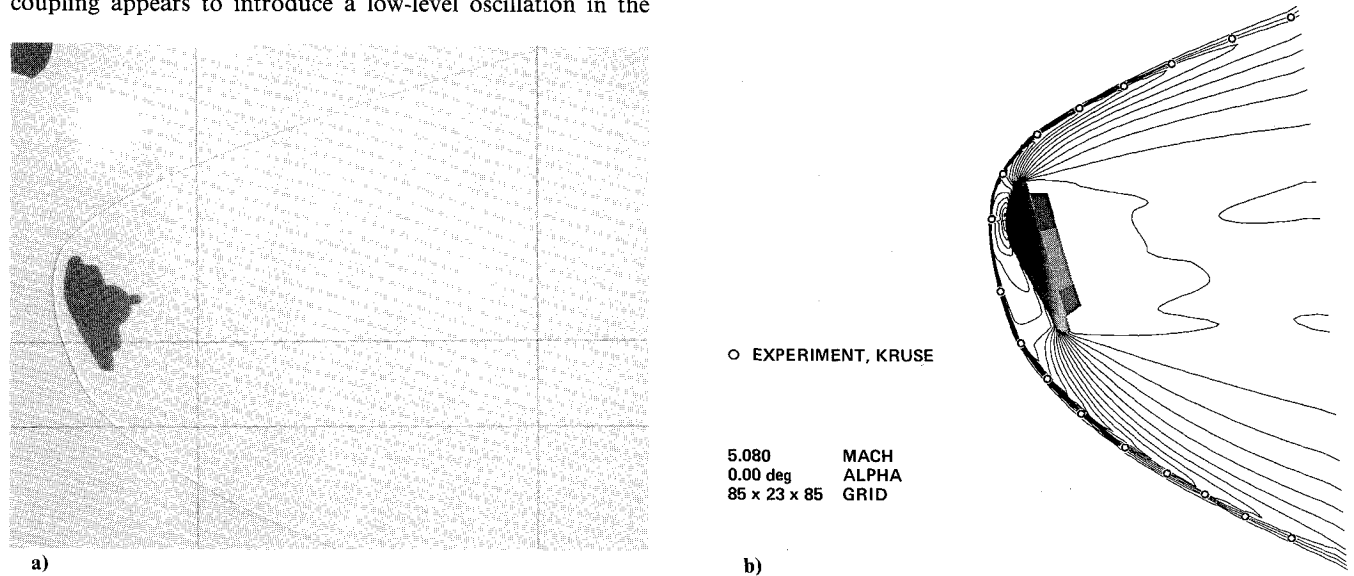5.080 MACH
0.00 deg ALPHA
85 x 23 x 85 GRID

a) b)

Fig. 3 Shock shape comparison, AFE model at Mach 5.08: a) ballistic range shadowgraph, Kruse and b) experimental and computed shock shapes.
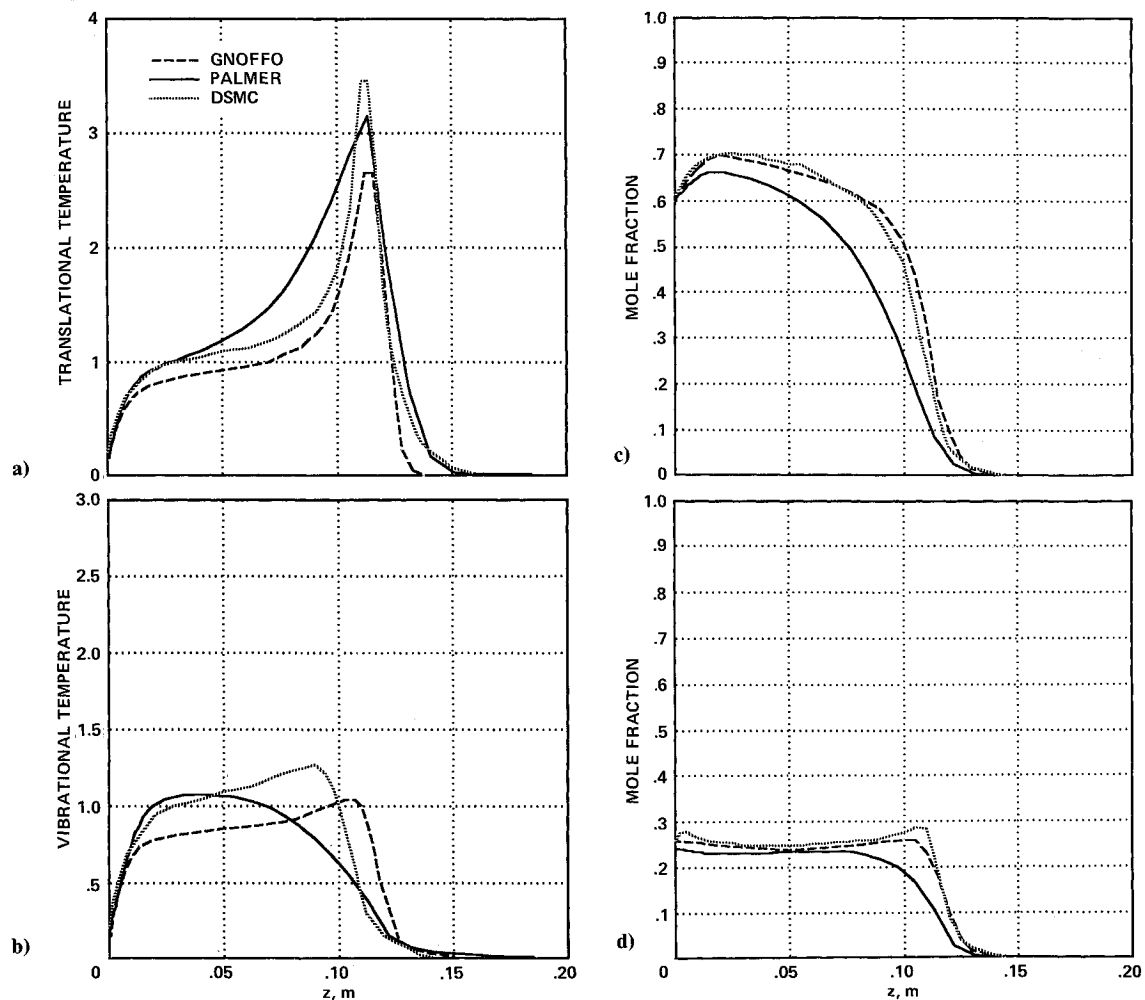

Fig. 4 Comparison of AFE results near stagnation streamline: a) translational temperature; b) vibrational temperature; c) atomic nitrogen mole fraction; and d) atomic oxygen mole fraction.
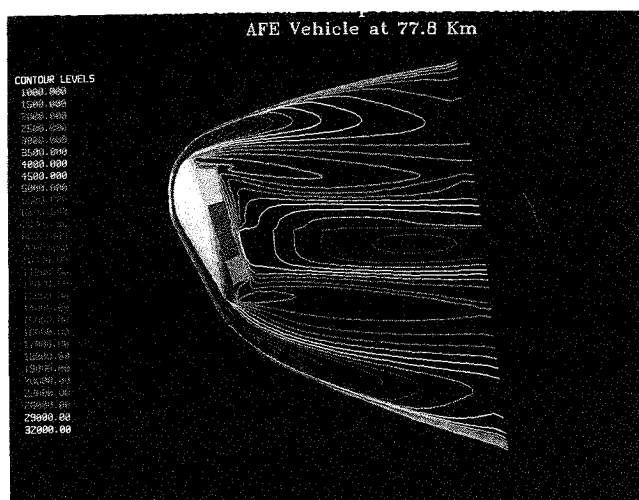
Fig. 5 Translational temperature contours, AFE vehicle at 77.8 km.

they are no longer changing, and comparisons against experimental and computational data indicate that the present method accurately computes hypersonic flows.

Results for the AFE

Ballistic range experiments using a 1.775-in.-diam scale model of the AFE were conducted by Bob Kruse at NASA Ames. The maximum Mach number attained was 5.08. The scale model had a hemisphere attached to its back representing a rocket engine that will be jettisoned before the aerobrake maneuver. Bow shock wave shapes were compared between the experimental shadowgraph shown in Fig. 3a and a numerical computation of the flowfield.

Figure 3b shows computed normalized density contours. Superimposed on these are circles representing the location of the bow shock from the shadowgraph. The experimental and computational bow shock locations are nearly identical.

The three-dimensional explicit code was then applied to the AFE vehicle at a trajectory point where the AFE is at an altitude of 77.8 km traveling at 8914 m/s. A $85 \times 23 \times 85$ grid constructed in three patches was used for the computation.

A constant temperature of 1650 K was imposed on the AFE forebody as a wall boundary condition. This temperature was chosen to compare results against previous computations. The temperature on the back of the AFE was held fixed at 750 K. In the skirt region, the wall temperature was blended from 750 to 1650 K.

Figures 4a–4d show data near the forebody singular line. Compared against the present results are those from Gnoffo et al.[11] using a point-implicit method and a direct-simulation Monte Carlo (DSMC) solution from Moss et al.[17] Neither Gnoffo et al. or Moss et al. performed a three-dimensional calculation but instead used an axisymmetric approximation to the AFE. They also used eleven species, the seven species considered in the present work plus four additional positive ions.

The computed translational and vibrational temperatures near the stagnation streamline are plotted in Fig. 4a. The three methods predict similar shock standoffs. The magnitude of the peak translational temperature is different, but the peak translational temperature is strongly influenced by the grid resolution in the peak region. A smaller grid spacing tends to give a higher peak temperature. The peak vibrational temperature predicted by the present explicit code occurs closer to the body than either the point-implicit or DSMC calculations, but in general the temperature distributions near the stagnation streamline predicted by the three methods are quite similar.

The next two figures show species mole fraction distributions near the stagnation streamline for N and O. The general

features of the curves are identical. There is a closer agreement between the point-implicit and DSMC computations, but both these calculations used the same chemical model. Taking into account the differences in methodology, species considered, and grids used, the agreement between the three calculations is encouraging.

Translational temperature contours are displayed in Fig 5. The highest temperatures exist in the bow shock near the forebody stagnation streamline. Temperature declines as the flow expands around the body, and in and behind the skirt area the temperature is quite low. In the subsonic base flow region between the shear layers, the temperature increases with the highest temperature in the area where the shear layers meet. Separation vortices and a large region of reverse flow, pronounced three-dimensional effects, are evident in the base region of the AFE. One of the effects of the reverse flow in the base region is the appearance of higher temperatures in the bottom half of the afterbody. The reverse current takes hot gas from the interior of the base flow area and directs it to the back of the AFE. This can be seen in the temperature contour plot.

As the flow expands around the lip of the AFE, the chemical composition freezes. A large region of strong nonequilibrium is evident in the expansion region behind the shoulder. The temperature in this area is low, between 1000 and 2000 K, but the amount of dissociation remains high. This indicates that the gas does not recombine as would be expected at such a low temperature and remains very much out of equilibrium. The physics and fluid dynamics in the base region appear to be quite complex. Accurately computing the base flow will prove a formidable challenge.

The AFE flowfield solution using the vectorized version of the code required about 15,000 iterations and consumed 45 h of CPU time on a Cray-2 supercomputer. The code's efficiency was approximately 6.5×10^{-5} s/point/iteration.

Concluding Remarks

The explicit code described in this study was simple to construct and has proven its ability to accurately compute flows in thermochemical nonequilibrium. The code was easily modified to handle complex geometries. The benefits of the explicit formulation are particularly evident when patched grid systems such as those used in the AFE calculations are employed.

The algorithm accurately computes hypersonic flow as demonstrated by the comparisons against experimental and numerical data. The value of the scaling quantity *tol* does not affect the final solution and if the value is high enough, does not affect the convergence rate of the solution. The solutions generated by the code exhibit very little grid sensitivity.

The code was successfully applied to the AFE vehicle at a flight trajectory point. Results were in close agreement with those calculated by others using two different methods. The fact that three different calculations yielded similar results generates confidence in the accuracy of the solution. An examination of the base flow region indicates areas of recirculation and reverse flow that significantly affect the thermodynamic state and chemical composition of the gas. The flowfield computations described in this work will be used in the design of the experiments to be carried aboard the AFE.

References

[1]Park, C., "Assessment of Two-Temperature Kinetic Model for Ionizing Air," AIAA Paper 87-1574, June 1987.

[2]Candler, G., "The Computation of Weakly Ionized Hypersonic Flows in Thermochemical Nonequilibrium," Ph.D. Thesis, Stanford University, Palo Alto, CA, 1988.

[3]Vincenti, W. G., and Kruger, C. H., *Physical Gas Dynamics*, 1st ed., Krieger Publishing Co., FL, 1965, pp. 15–21.

[4]Hirschfelder, J. O., Curtiss, C. F., and Bird, R. B., *Molecular Theory of Gases and Liquids*, 2nd ed., Wiley, New York, 1954, pp. 514–540.

[5]Candler, G., and MacCormack, R., "The Computation of Hypersonic Ionized Flows in Chemical and Thermal Nonequilibrium," AIAA Paper 88-0511, Jan. 1988.

[6]Wilke, C. R., "A Viscosity Equation for Gas Mixtures," *Journal of Chemical Physics,* Vol. 18, No. 4, 1950, p. 517.

[7]Oran, E. S., and Boris, J. P., *Numerical Simulation of Reactive Flow,* 1st ed., Elsevier, New York, 1987, pp. 252–261.

[8]Park, C., "On Convergence of Computation of Chemically Reacting Flows," AIAA Paper 85-0247, Jan. 1985.

[9]Anderson, W. K., Thomas, J. L., and Van Leer, B., "Comparison of Finite Volume Flux Vector Splittings for the Euler Equations," *AIAA Journal,* Vol. 24, No. 9, 1986, pp. 1453–1460.

[10]Palmer, G. E., "An Improved Flux-Split Algorithm Applied to Hypersonic Flows in Chemical Equilibrium," AIAA Paper 88-2693, June 1988.

[11]Gnoffo, P. A., Gupta, R. N., and Shinn, J. L., "Conservation Equations and Physical Models for Hypersonic Air Flows in Thermal and Chemical Nonequilibrium," NASA TP 2867, Feb. 1989.

[12]Yee, H. C., and Shinn, J. L., "Semi-Implicit and Fully Implicit Shock-Capturing Methods for Hyperbolic Conservation Laws with Stiff Source Terms," AIAA Paper 87-1116, June 1987.

[13]Candler, G., "On the Computation of Shock Shapes in Nonequilibrium Hypersonic Flows," AIAA Paper 89-0312, June 1989.

[14]Jones, W. L., and Cross, A. E., "Electrostatic-Probe Measurements of Plasma Parameters for Two Reentry Flight Experiments at 25,000 Feet Per Second," NASA TN D-6617, Feb. 1972.

[15]Lobb, R. K., "Experimental Measurement of Shock Detachment Distance on Spheres Fired in Air at Hypervelocities," *The High Temperature Aspects of Hypersonic Flow,* AGARD-NATO Specialists Meeting, Vol. 1, 1962, pp. 519–527.

[16]Palmer, G., "An Efficient, Explicit Finite-Rate Algorithm to Compute Flows in Chemical Nonequilibrium," AIAA Paper 89-0522, 1989.

[17]Moss, J. N., Bird, G. A., and Virendra, K. D., "Nonequilibrium Thermal Radiation for an Aeroassist Flight Experiment Vehicle," AIAA Paper 88-0081, Jan. 1988.

Clark H. Lewis
Associate Editor